crystals

MDPI

Article

Luminescent Arylalkynyltitanocenes: Effect of Modifying the Electron Density at the Arylalkyne Ligand, or Adding Steric Bulk or Constraint to the Cyclopentadienyl Ligand

Matilda Barker [1], Samantha C. Walter [1], Elizabeth A. McCallum [1], River S. Golden [1], John H. Zimmerman [1], Jackson S. McCarthy [1], Colin D. McMillen [2,*] and Paul S. Wagenknecht [1,*]

[1] Department of Chemistry, Furman University, Greenville, SC 29613, USA
[2] Department of Chemistry, Clemson University, Clemson, SC 29634, USA
* Correspondence: cmcmill@clemson.edu (C.D.M.); paul.wagenknecht@furman.edu (P.S.W.)

Abstract

Photocatalysis using complexes of d^0 metals with ligand-to-metal charge-transfer (LMCT) excited states is an active area of research. Because titanium is the second most abundant transition metal in the earth's crust, d^0 complexes of Ti^{IV} are an appropriate target for this research. Recently, our group has demonstrated that the arylethynyltitanocene $Cp_2Ti(C_2Ph)_2CuBr$ is not emissive in room-temperature fluid solution, whereas the corresponding Cp* complex, $Cp^*_2Ti(C_2Ph)_2CuBr$, is emissive. The Cp* ligand is hypothesized to provide steric constraint that inhibits excited-state structural rearrangement. However, modifying the structure also changes the orbital character of the excited state. To investigate the impact of the excited-state orbital character on the photophysics, herein we characterize complexes similar to $Cp^*_2Ti(C_2Ph)_2CuBr$—but one with a more electron-rich arylethynyl ligand, ethynyldimethylaniline (C_2DMA), and one with a more electron-poor arylethynyl ligand, ethynyl-α,α,α-trifluorotoluene. We have also prepared complexes with the C_2DMA ligand but with different Cp ligands that adjust the steric bulk and constraint around the Ti, by replacing the Cp* ligands with either indenyl ligands or an *ansa*-cyclopentadienyl ligand where the two Cp ligands are bridged by a dimethylsilylene. All four target complexes have been characterized crystallographically and structure activity relationships are highlighted.

Keywords: photosensitizer; titanocene; phosphorescence; first-row transition metal; rigidoluminescence

Academic Editor: Nabeen K Shrestha

Received: 25 July 2025
Revised: 13 August 2025
Accepted: 18 August 2025
Published: 21 August 2025

Citation: Barker, M.; Walter, S.C.; McCallum, E.A.; Golden, R.S.; Zimmerman, J.H.; McCarthy, J.S.; McMillen, C.D.; Wagenknecht, P.S. Luminescent Arylalkynyltitanocenes: Effect of Modifying the Electron Density at the Arylalkyne Ligand, or Adding Steric Bulk or Constraint to the Cyclopentadienyl Ligand. *Crystals* **2025**, *15*, 745. https://doi.org/10.3390/cryst15080745

1. Introduction

The use of solar energy to drive uphill reactions for the synthesis of fuels [1–3] or other organic materials [4–8] requires photocatalysts that, upon absorption of light, have excited states with lifetimes sufficient to undergo bimolecular energy- or electron-transfer. Photocatalysts are also used in applications such as dye-sensitized solar cells [9–11], photon upconversion [12,13], and singlet oxygen generation [14]. Transition-metal complexes of ruthenium and iridium have dominated the field of photocatalysis, but recently there has been significant interest in developing complexes of earth-abundant metals, particularly of first-row transition metals [15–19]. One challenge with the use of first-row transition metals is that low-energy, metal-centered (MC) excited states, i.e., excited states resulting from electronic transitions between d orbitals, are typically accessible from the photoactive state [20]. Because of the very short lifetime of such MC states, access to these states signifi-

cantly decreases the excited-state lifetimes and such complexes are either non-emissive or the emission has a very short lifetime.

Recently, there has been interest in overcoming this obstacle by using complexes of d^0 metals with ligand-to-metal charge-transfer (LMCT) excited states [21]. The d^0 electron configuration eliminates the presence of MC states. Recently several Zr^{IV} complexes have been shown to be emissive in room-temperature (RT) fluid solution with lifetimes in the microsecond range, some having utility as photocatalysts [22–28]. However, the corresponding Ti^{IV} complexes have not been emissive [22,26,28]. In 2022, our group demonstrated that **^{Ph}[Ti]** (Figure 1) is weakly emissive in RT fluid solution with a photoluminescent quantum yield, $\Phi_{PL} = 2 \times 10^{-4}$. However, this complex is extremely sensitive to photodecomposition with a photodecomposition quantum yield, $\Phi_{decomp} = 0.65$. Coordination of CuBr between the alkynes to give **^{Ph}[Ti]CuBr** (Figure 1) improved the photostability ($\Phi_{decomp} = 1.2 \times 10^{-3}$), but resulted in a complex that is non-emissive [29]. In 2023, we demonstrated that replacement of the cyclopentadienyl ligand with pentamethylcyclopentadienyl, Cp*, to give **^{Ph}[Cp*Ti]CuBr** (Figure 1) resulted in a complex that is reasonably photostable ($\Phi_{decomp} = 0.015$) and emissive in RT tetrahydrofuran (THF) solution ($\Phi_{PL} = 1.3 \times 10^{-3}$, $\tau = 0.18$ μs). We hypothesized that the increased steric bulk of the Cp* ligand restricted excited-state distortion, thus decreasing the rate of nonradiative decay and that this was responsible for the improved emission characteristics [30]. To further test this hypothesis, we prepared a complex with ortho-methyl substituents on the phenyl ring to give the xylyl complex, **^{xyl}[Cp*Ti]CuBr** (Figure 1). This xylyl complex is also reasonably photostable and has an emission quantum yield and excited-state lifetime approximately an order of magnitude greater than the phenyl analog ($\Phi_{PL} = 1.2 \times 10^{-2}$, $\tau = 1.5$ μs). This complex was also shown to sensitize molecular photon upconversion and singlet oxygen formation [31].

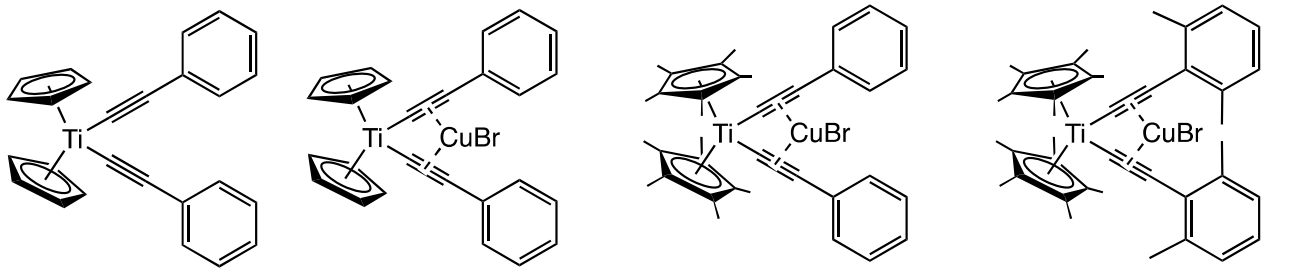

Figure 1. Previous arylethynyltitanocenes investigated along with the abbreviations used herein and their photoluminescent quantum yields (Φ_{PL}), emission lifetimes (τ), and photodecomposition quantum yields (Φ_{decomp}) in deaerated THF. Figure adapted from [31].

Several open questions remain. Modifying the complex often changes the identity of the excited state. For example, whereas the excited state of the non-emissive **^{Ph}[Ti]CuBr** is dominated by a combination of C_2Ph-to-Ti LMCT and CuBr-to-Ti metal halide-to-metal CT (MXMCT), the Cp* version, **^{Ph}[Cp*Ti]CuBr**, has significant Cp*-to-Ti LMCT character [30]. How does this shift in excited-state character change the excited-state behavior? And, are there other means to provide steric restriction that might give similar excited-state behavior as the Cp* ligand? To investigate these questions, we have prepared complexes similar to **^{Ph}[Cp*Ti]CuBr**—but one with a more electron-rich arylethynyl ligand, ethynyldimethylaniline, **^{DMA}[Cp*Ti]CuBr**, and one with a more electron-poor arylethynyl ligand, ethynyl-α,α,α-trifluorotoluene, **^{PhCF3}[Cp*Ti]CuBr** (Figure 2). We have also prepared complexes

with the ethynyldimethylaniline (C_2DMA) ligand but with different Cp ligands that adjust the steric bulk and constraint around the Ti, namely the indenyl complex, **^{DMA}[IndTi]CuBr**, and an *ansa*-titanocene **^{DMA}[*ansa*-CpTi]CuBr** (Figure 2). All four complexes have been characterized by single-crystal X-ray diffraction.

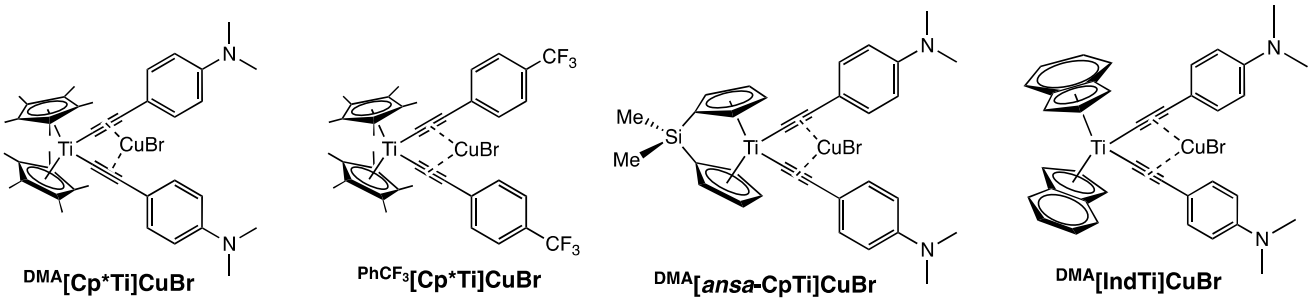

Figure 2. New titanocenes prepared herein along with the abbreviations used in the discussion. The superscripted **DMA** indicates the dimethylaniline substituent on the alkynes; the superscripted **PhCF$_3$** indicates the α,α,α-trifluorotoluene substituent on the alkynes. **Ind** indicates the indenyl ligand, **Cp*** the pentamethylcyclopentadienyl ligand, and ***ansa*-Cp** the $Me_2Si(\eta^5\text{-}C_5H_4)_2$ ligand.

2. Materials and Methods

2.1. General Methods

UV-Vis: Absorption spectra were collected using a Varian (Walnut Creek, CA, USA) Cary-50 UV–vis spectrophotometer.

Emission Spectra: Emission spectra were collected using a Horiba Scientific (Piscataway, NJ, USA) Fluorolog-3 spectrofluorometer equipped with a FL-1013 liquid nitrogen dewar assembly for 77 K measurements. Emission spectra at 77 K were performed in 2-methyltetrahydrofuran (2-Me-THF) glass. All emission spectra were corrected for the response factor of the R928 photomultiplier tube using the factory correction files. Emission spectra in room-temperature solution were additionally corrected with blank subtraction.

Excitation spectra: Excitation spectra were collected using a Horiba Scientific Fluorolog-3 sprectrofluorometer.

Emission Lifetime: Emission lifetimes were measured using a Photon Technology International (PTI, Lawrenceville, NJ, USA) GL-3300 pulsed nitrogen laser fed into a PTI GL-302 dye laser as the excitation source. The resulting data set was collected on an OLIS (Athens, GA, USA) SM-45 EM fluorescence lifetime measurement system using a Hamamatsu R928 photomultiplier tube fed through a variable feed-through terminator into a LeCroy (Chestnut Ridge, NY, USA) WaveJet 352A oscilloscope and analyzed using OLIS Spectral Works. Double exponential fits were performed using WaveMatrics (Lake Oswego, OR, USA) IGOR Pro 9.

NMR spectra: ^{1}H NMR spectra were obtained using a JEOL (Peabody, MA, USA) JNM-ECZR (500 MHz) spectrometer.

Infrared spectra: Vibrational spectra were performed on a PerkinElmer (Shelton, CT, USA) Spectrum Two FT-IR spectrometer using a universal attenuated total reflection accessory.

Elemental analysis: Elemental analyses were performed by Midwest Microlabs (Indianapolis, IN, USA).

Quantum Yields of Photoluminescence (Φ_{PL}): Relative solution-state photoluminescence quantum yields were determined in THF against a $[Ru(bpy)_3]^{2+}$ standard in air-saturated CH_3CN (Φ_{PL} = 0.018) [32]. The absorbance of the analyte and $[Ru(bpy)_3]^{2+}$ solutions were matched at the wavelength of excitation (450 nm), and the reported quantum yields are averages of at least three replicates.

Quantum Yields of Photodecomposition (Φ_{decomp}): The quantum yields for photodecomposition were determined using the previously published method [31] and are detailed in the Supplementary Materials.

2.2. Computational Methods

DFT and TDDFT calculations used Gaussian 16 [33] and were performed according to the literature [31], using GaussView 6.32 [34] for images of orbitals, and GaussSum 3.0 [35] for Mulliken population analysis. The computational model for DFT and TDDFT used B3LYP [36,37] and 6-311+G(d) [38–42] including a Tomasi polarizable continuum (PCM) model using the dielectric constant for THF [43].

2.3. Single-Crystal X-Ray Diffraction

Crystals of ^{DMA}**[Cp*Ti]CuBr** and ^{PhCF3}**[Cp*Ti]CuBr** were grown by slow evaporation of THF. Crystals of ^{DMA}**[IndTi]CuBr** were grown by slow evaporation of dichloromethane. Crystals of ^{DMA}***[ansa*-CpTi]CuBr** were grown by dissolving the complex in THF and allowing diethylether to diffuse the solution (vapor-phase). In each case, triethylamine (5% v/v) was added to the solvent to protect against acid hydrolysis. Single-crystal X-ray diffraction data were collected at 100 K using a Bruker (Madison, WI, USA) D8 Quest diffractometer. The data were collected using phi and omega scans (0.5° frame width) with a Mo Kα (λ = 0.71073 Å) microfocus source and a Photon 3 detector. Data were processed (SAINT) and corrected for absorption (multi-scan, SADABS), using the Bruker Apex4 suite [44]. The structures were solved by intrinsic phasing (SHELXT) and subsequently refined by full matrix least squares on F^2(SHELXL) [45,46]. Reflections obscured by the beamstop were omitted from the refinements. All non-hydrogen atoms were refined anisotropically. Hydrogen atoms attached to carbon atoms were refined in calculated positions using riding models where $U_{eq}(H) = 1.2U_{eq}(C)$ for aromatic C–H and $U_{eq}(H) = 1.5U_{eq}(C)$ for methyl C–H. The structure of ^{PhCF3}**[Cp*Ti]CuBr** was found to be a THF solvate, and THF was included in the structural model without restraints. In ^{DMA}**[IndTi]CuBr** and ^{DMA}***[ansa*-CpTi]CuBr** the bromine site was found to support mixed occupancy of Br and OH. These were refined in separate, nearby positions with the site occupancies refined as free variables. In ^{DMA}**[IndTi]CuBr** this resulted in a ratio of 0.814(4):0.186(4) for Br:OH, and in ^{DMA}***[ansa*-CpTi]CuBr** this resulted in a ratio of 0.673(5):0.327(5) for Br:OH. The structure of ^{DMA}***[ansa*-CpTi]CuBr** was refined in a noncentrosymmetric space group ($Pna2_1$) with a corresponding absolute structure parameter of 0.041(18). Crystallographic data are summarized in Table 1. Crystallographic data for the complex ^{DMA}**[IndTi]CuBr$_{0.29}$(OH)$_{0.71}$**, differing from ^{DMA}**[IndTi]CuBr** in the degree of Br/OH substitution, are reported in the Supplementary Information, Table S1. CCDC 2475385-2475389 contains the complete supplementary crystallographic data for this paper and can be obtained from the Cambridge Crystallographic Data Centre.

Table 1. Crystallographic data and refinement details.

	^{PhCF_3}**[Cp*Ti]CuBr THF**	^{DMA}**[Cp*Ti]CuBr**	^{DMA}**[IndTi]CuBr**	^{DMA}**[*ansa*-CpTi]CuBr**
empirical formula	$C_{42}H_{46}BrCuF_6OTi$	$C_{40}H_{50}BrCuN_2Ti$	$C_{38}H_{34.19}Br_{0.81}CuN_2O_{0.19}Ti$	$C_{32}H_{34.33}Br_{0.67}CuN_2O_{0.33}SiTi$
formula wt. (g/mol)	872.14	750.17	698.07	645.29
crystal system	triclinic	monoclinic	monoclinic	orthorhombic
space group, *Z*	*P*-1	$P2_1/c$, 8	$P2_1/c$, 4	$Pna2_1$, 4
temperature (K)	100(2)	100(2)	100(2)	100(2)
a (Å)	9.4166(4)	15.5719(8)	6.6123(5)	22.7878(15)
b (Å)	13.8760(6)	16.9073(9)	23.8625(17)	9.3747(6)
c (Å)	15.7364(6)	27.5471(14)	19.5013(14)	13.6177(9)
α (°)	75.7461(18)	90	90	90
β (°)	74.2782(18)	103.5177(17)	97.482(2)	90
γ (°)	74.9301(19)	90	90	90
volume (Å^3)	1876.72(14)	7051.7(6)	3050.8(4)	2090.1(3)
D_{calc} (g/cm^3)	1.543	1.413	1.520	1.473
crystal size (mm)	0.04 × 0.08 × 0.10	0.07 × 0.08 × 0.10	0.02 × 0.10 × 0.20	0.07 × 0.08 × 0.10
abs. coeff. (mm^{-1})	1.907	1.993	2.051	1.992
F(000)	892	3120	1428	1326
Tmax, Tmin	1.000, 0.923	1.000, 0.951	1.000, 0.858	1.000, 0.510
Θ range for data (°)	3.14 to 25.73	1.94 to 26.03	2.27 to 25.70	3.81 to 25.70
reflections coll.	79,466	207,807	53,511	41,647
data/restr./param.	7140/0/479	13,887/0/839	5768/2/399	5502/2/354
R(int)	0.1487	0.1311	0.1861	0.0947
final R [$I > 2\sigma(I)$] R1, wR2	0.0544, 0.1021	0.0465, 0.1024	0.0603, 0.1219	0.0471, 0.0985
final R (all data) R1, wR2	0.0797, 0.1220	0.0954, 0.1253	0.1223, 0.1510	0.0632, 0.1075
goodness-of-fit on F^2	1.067	1.015	1.015	1.033
larg. diff. peak, hole (eÅ^{-3})	0.780, −0.641	1.243, −1.103	0.862, −0.780	0.738, −0.320
CCDC Deposition No.	2475385	2475386	2475387	2475388

2.4. Syntheses

Diethylether and THF were dried and degassed using an Innovative Technology (Newburyport, MA, USA) PureSolv solvent purification system before use. All other materials were used as received. All reactions were performed under an inert atmosphere using standard Schlenk techniques. Dichlorobis(indenyl) titanium(IV), copper(I)bromide, *n*-butyllithium, 4-ethynyl-*α*,*α*,*α*-trifluorotoluene, and 4-ethynyl-*N*,*N*-dimethylanaline were purchased from Sigma Aldrich (St. Louis, MO, USA). Bis-(pentamethylcyclopentadienyl)titanium dichloride was purchased from Strem Chemicals (Newburyport, MA, USA). [$Me_2Si(\eta^5$-$C_5H_4)_2TiCl_2$], *ansa*-Cp_2TiCl_2, was prepared according to the literature method [47]. ^{DMA}**[Cp*Ti]** was prepared by a modification of the literature procedure [48] where THF was substituted for diethylether (Supplementary Materials).

General synthetic method for the parent titanocenes: An oven-dried, two-necked round-bottom flask was purged with argon and then charged with dried, degassed solvent and the appropriate alkyne. The solution was stirred and chilled to −78 °C (dry ice/acetone) for 10 min. Next, *n*-butyllithium (2.5 M in hexanes) was added via syringe and the solution was stirred for an additional 10 min at −78 °C. The cooling bath was removed and the solution was stirred for an additional 10 min. The appropriate titanocene was then added and the mixture was stirred at RT for 4 hrs in the dark. Following filtration, the product was purified as detailed for each complex.

General method for coordination of CuBr: An oven-dried, two-necked round-bottom flask was purged with argon and charged with the parent titanocene and CuBr. Following injection of dried, degassed solvent, the reaction mixture was stirred in the dark at RT for 3–4 h and then purified as detailed for each complex.

^{DMA}[Cp*Ti]CuBr: The general method for coordination of CuBr was followed using **^{DMA}[Cp*Ti]** (139 mg, 0.23 mmol, 1.0 equiv), CuBr (70 mg, 0.49 mol, 2.1 equiv) and THF (16 mL) Following a 3h reaction period the mixture was filtered (removing CuBr). The solvent was evaporated from the deeply colored filtrate. THF (2 mL) was added to the dried product, and the flask was sonicated in a cleaning bath and cooled at −20 °C for 1.5 h. The solid was filtered, rinsed with hexanes, and dried in vacuo (75 mg, 44%). UV–Vis (THF) λ_{max} (ε); 546 (9770), 360 sh (18,800), 287 (47,500). ^{1}H NMR (500 MHz, $CDCl_3$) δ 7.52 (d, 4H), 6.67 (d, 4H), 2.97 (s, 12H), 1.97 (s, 30H); Anal. Calcd (found) for $C_{40}H_{50}N_2TiCuBr\bullet\frac{1}{2}H_2O$: C, 63.28 (63.19); H, 6.77 (6.76); N, 3.69 (3.50). IR (neat) $\nu_{C\equiv C}$ = 1985, 1969 cm^{-1}, $\nu_{O\text{-}H}$ (from water) = 3427, 3519 cm^{-1} (very weak).

^{PhCF_3}[Cp*Ti]: The general procedure for the parent titanocenes was followed using THF (8 mL), 4-ethynyl-α, α, α-trifluorotoluene (0.25 mL, 1.5 mmol, 4 equiv), *n*-butyllithium (2.5 M, 0.68 mL, 1.7 mmol, 4.4 equiv) and $Cp^*_2TiCl_2$ (150 mg, 0.385 mmol, 1.0 equiv). After the 4 h reaction period, impurities were removed via vacuum filtration, and the solvent was removed from the deep-red filtrate using rotary evaporation. The resulting solid was loaded onto a silica gel column (1 cm × 13 cm) and eluted using 5% (v/v) mixture of triethylamine in dichloromethane. A red band was eluted into a round-bottom flask, and the solvent was evaporated. Hexanes (4 mL) were then added to the flask. Following sonication of the flask in a cleaning bath and cooling (dry ice) the solid was filtered and dried in vacuo (147 mg, 57%). UV-Vis (THF) λ_{max} (ε); 538 (1410), 476 (2140), 373 (7980), 346 (10,600), 301 (32,700). ^{1}H NMR (500 MHz, $CDCl_3$) δ 7.47 (d, 4H), 7.36 (d, 4H), 2.06 (s, 30H). Anal. Calcd (found) for $C_{38}H_{38}TiF_6$: C, 69.51 (69.67); H, 5.83 (6.16). IR (neat) $\nu_{C\equiv C}$ = 2075 cm^{-1}.

^{PhCF_3}[Cp*Ti]CuBr: The general method for coordination of CuBr was followed using **^{PhCF_3}[Cp*Ti]** (50 mg, 0.076 mmol, 1.0 equiv), CuBr (22 mg, 0.15 mmol, 2.0 equiv), and CH_2Cl_2 (6 mL). After a 4 h reaction period, the mixture was filtered through Celite (to remove CuBr) and the filtrate collected. The solvent was removed using rotary evaporation. Dichloromethane (0.5 mL) was added to partially dissolve the product which was then precipitated by the addition of hexanes (8 mL). The mixture was cooled in dry ice for 10 min, and the solid was filtered and dried in vacuo (42 mg, 70%). UV-Vis (THF) λ_{max} (ε); 460 (4680), 375 (9250). ^{1}H NMR (500 MHz, $CDCl_3$) δ 7.81 (d, 4H), 7.60 (d, 4H), 1.97 (s, 30H) Anal. Calcd (found) for $C_{38}H_{38}TiF_6CuBr\bullet 3H_2O$: C, 53.44 (53.11); H, 5.19 (4.87). IR (neat) $\nu_{C\equiv C}$ = 1960 cm^{-1}, $\nu_{O\text{-}H}$ (from water) = 3426, 3519 cm^{-1}.

^{DMA}[ansa-CpTi]: The general procedure for the parent titanocenes was followed using Et_2O (8 mL), 4-ethynyl-*N*,*N*-dimethylaniline (169 mg, 1.17 mmol, 2.5 equiv), *n*-butyllithium (2.5 M, 0.47 mL, 1.2 mmol, 2.5 equiv) and [$Me_2Si(\eta^5\text{-}C_5H_4)_2TiCl_2$] (150 mg, 0.469 mmol, 1.0 equiv). After the 4 h reaction period, the reaction mixture was chilled to −20 °C for 30 min and then immediately filtered through a Hirsch funnel. The precipitate was loaded onto an alumina (neutral, Grade I, ~60 mesh) column (2 cm × 15 cm) and eluted using a 5% (v/v) mixture of triethylamine in CH_2Cl_2. The dark purple band was eluted into a round-bottom flask and the solvent was evaporated. THF (1 mL) was added to partially dissolve the product and hexanes (25 mL) was added to precipitate the product. Following sonication of the flask in a cleaning bath and then cooling to −20 °C for 1 h, the product was filtered and dried in vacuo (145 mg, 58%). UV-Vis (THF) λ_{max} (ε); 548 (20,100), 450 sh (11,700). ^{1}H NMR (500 MHz, $CDCl_3$) δ 7.48 (t, 4H), 7.21 (d, 4H), 6.58 (d, 4H), 5.72 (t, 4H), 2.94 (s, 12H), 0.56 (s, 6H). Anal. Calcd (found) for $C_{32}H_{34}N_2SiTi$: C, 73.55 (73.39); H, 6.56 (6.76); N 5.36 (5.49). IR (neat) $\nu_{C\equiv C}$ = 2044, 2024 cm^{-1}.

^{DMA}[ansa-CpTi]CuBr: The general method for coordination of CuBr was followed using **^{DMA}[ansa-CpTi]** (100 mg, 0.186 mmol, 1.0 equiv), CuBr (67 mg, 0.47 mmol, 2.5 equiv) and THF (10 mL). After a 3 h reaction period, the solvent was removed using rotary evaporation. The resulting solid was then purified on a silica gel column (2 cm × 15 cm) with 2% (v/v) triethylamine in CH_2Cl_2 as the eluent. The dark-blue band was eluted into a round-bottom flask and the solvent was evaporated. Hexanes (10 mL) was added, and the flask was sonicated in a cleaning bath, and cooled to −20 °C for 30 min. The solid was filtered and dried in vacuo (89 mg, 71%). UV-Vis (THF) λ_{max} (ε); 583 (11,200), 400 (19,000), 383 sh (18,700). ^{1}H NMR (500 MHz, $CDCl_3$) δ 7.43 (d, 4H), 6.64 (d, 4H), 6.50 (t, 4H), 5.80 (t, 4H), 2.99 (s, 12H), 0.65 (s, 6H). Anal. Calcd (found) for $C_{32}H_{34}N_2SiTiCuBr_{0.67}(OH)_{0.33}$: C, 59.56 (59.87); H, 5.36 (5.56); N 4.34 (4.50). Calcd for $C_{32}H_{34}N_2SiTiCuBr•½C_6H_{14}$: C, 59.28; H, 5.83; N 3.95. IR (neat) $\nu_{C\equiv C}$ = 1996, 1940 cm^{-1}.

^{DMA}[IndTi]: The general procedure for the parent titanocenes was followed using Et_2O (8 mL), 4-ethynyl-*N*,*N*-dimethylaniline (137 mg, 0.946 mmol, 2.2 equiv), *n*-butyllithium (2.5 M, 0.38 mL, 0.95 mmol, 2.2 equiv), and Ind_2TiCl_2 (150 mg, 0.430 mmol, 1.0 equiv). After the 4 h reaction period, the solid was collected via vacuum filtration and was loaded onto a silica gel column (2 cm × 15 cm) and eluted using a 5% (v/v) mixture of triethylamine in CH_2Cl_2. The purple band was eluted into a round-bottom flask, and the solvent was evaporated. CH_2Cl_2 (1 mL) was added to partially dissolve the product which was then precipitated by the addition of hexanes (20 mL). The flask was briefly sonicated in a cleaning bath and the solid was filtered and dried in vacuo (123 mg, 49.2%). UV-Vis (THF) λ_{max} (ε); 558 (16,000), 448 (12,000), 285 (64,300). ^{1}H NMR (500 MHz, C_6D_6) δ 7.57 (m, 4H), 7.50 (d, 4H), 6.98 (m, 4H), 6.48 (d, 4H), 6.39 (t, 2H), 6.28 (d, 4H), 2.42 (s, 12H). Anal. Calcd (found) for $C_{38}H_{34}N_2Ti•H_2O$: C, 78.08 (78.12); H, 6.21 (6.22); N, 4.79 (5.17). IR (neat) $\nu_{C\equiv C}$ = 2046, 2025 cm^{-1}, $\nu_{O\text{-}H}$ (from water) = 3390 cm^{-1} (broad).

^{DMA}[IndTi]CuBr: The general method for coordination of CuBr was followed using **^{DMA}[IndTi]** (100 mg, 0.177 mmol, 1.0 equiv), CuBr (51 mg, 0.35 mmol, 2.0 equiv), and THF (10 mL). After a 3 h reaction period, the solvent was evaporated, and the residue was purified on a silica gel column (2 cm × 15 cm) using 5% (v/v) triethylamine in CH_2Cl_2 as the eluent. The green band was eluted into a round-bottom flask, and the solvent was evaporated. CH_2Cl_2 (2 mL) was added to partially dissolve the product which was then precipitated by the addition of hexanes (20 mL). The mixture was cooled in dry ice and the solid was filtered and dried in vacuo (94 mg, 75%). UV-Vis (THF) λ_{max} (ε); 592 (9000), 401 (18,200), 291 (41,200). ^{1}H NMR (500 MHz, $CDCl_3$) δ 7.48 (m, 4H), 7.44 (d, 4H), 7.21 (m, 4H), 6.66 (d, 4H), 6.03 (d, 4H), 5.81 (t, 2H), 3.00 (s, 12H). Anal. Calcd (found) for $C_{38}H_{34}N_2TiCuBr$: C, 64.28 (63.88); H, 4.83 (5.03); N, 3.95 (4.04). IR (neat) $\nu_{C\equiv C}$ = 1981, 1969 cm^{-1}.

3. Results and Discussion

3.1. Syntheses and Spectroscopic Characterization

The syntheses were performed using the methods published previously for similar complexes [30,31,48]. Namely, to make the parent arylethynyltitanocenes, the appropriate arylacetylene was deprotonated with *n*-BuLi followed by addition of the appropriate titanocene dichloride (Figure 3). The syntheses of **^{DMA}[IndTi]** and **^{DMA}[*ansa*-CpTi]** were performed in Et_2O as has been employed for many related titanocenes [48]. However, the Cp* complex syntheses were performed in THF. Attempts in Et_2O resulted in poorer yields. Purification of these arylalkynyltitanocenes was performed by chromatography using an eluent of 5% Et_3N in CH_2Cl_2 (v/v). The addition of Et_3N follows previous reports and is necessary to prevent acid hydrolysis during column purification [29,49]. Silica gel was used as the stationary phase for all complexes except for **^{DMA}[*ansa*-CpTi]** which decomposed

on that support. Replacing silica gel with alumina resulted in a pure product. Following chromatography, each complex was recrystallized, resulting in analytically pure products. In all cases, the ^{1}H NMR spectra support the proposed structure of the parent compound (Supplementary Materials Figures S2, S4 and S6). The arylalkynyl complexes are air-stable but light-sensitive and can be handled on the bench top under reduced light conditions.

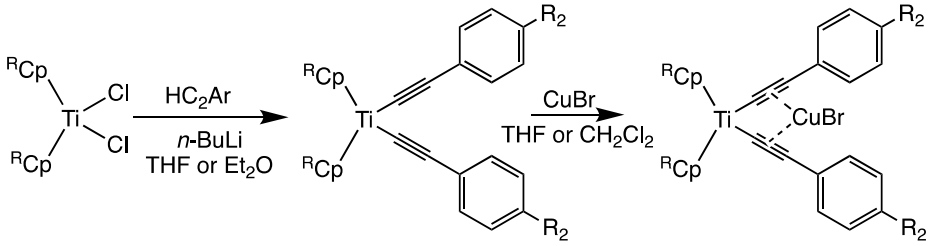

Figure 3. Synthetic scheme for the synthesis of arylethynyltitanocenes and the corresponding CuBr coordinated complexes. ^{R}Cp = Cp*, or indenyl, or *ansa*-Cp. R_2 = CF_3 or NMe_2.

The coordination of CuBr between the alkynes followed the procedure for related arylalkynyltitanocenes where excess CuBr was added to the appropriate parent complex (Figure 3) [29]. Upon stirring for 3–4 h, the sample was filtered and **^{DMA}[*ansa*-CpTi]CuBr** and **^{DMA}[IndTi]CuBr** were purified by chromatography on silica gel using an eluent of 2–5% (v/v) Et_3N in CH_2Cl_2, followed by recrystallization. The Cp* complexes were purified only by recrystallization similar to other Cp* complexes of this type [30,31]. In all cases, the ^{1}H NMR spectra of the complexes with CuBr coordinated between the alkynes have the same peaks and splittings as the parent complexes, but with slight shifts in the resonances (Supplementary Materials Figures S1–S7). Additional evidence of CuBr coordination is provided by the shift in the C≡C stretching frequency in the IR spectra (Supplementary Materials Figure S8). For all four complex pairs, there is a shift to lower energy of 50 to 115 cm^{-1} upon coordination of CuBr, consistent with the alkynes engaging in η^2 coordination with the metal [29,50,51].

For **^{DMA}[*ansa*-CpTi]CuBr**, the crystal structure revealed a substitution of 33% of the Br by OH (*vide infra*) and this ratio resulted in a reasonable agreement between the predicted and experimental values for the elemental analysis. However, solvation by ½ hexane molecule per formula unit also gives reasonable agreement (both are listed in the experimental) and is qualitatively supported by the presence of a hexanes peak at 0.88 ppm in the ^{1}H NMR spectrum. Furthermore, the ^{1}H NMR spectrum of **^{DMA}[*ansa*-CpTi]CuBr** is very sharp and does not reveal a second set of peaks attributable to the OH analog introduced by this substitution, suggesting that substitution occurred during crystal growth. Though we have not previously reported this substitution, we had observed such substitution previously but were able to obtain unsubstituted crystals by changing the crystal growth conditions. In those cases, we only published the unsubstituted structure, something we were unable to obtain herein. We believe that this substitution can also occur during the column purification, as an impurity was observed for **^{Ph}[Cp*Ti]CuBr** when purified by column chromatography [30] that we believe to be the OH analog. However, for **^{Ph}[Cp*Ti]CuBr** there was ^{1}H NMR evidence for the impurity. It is worth noting that in the case of **^{Ph}[Cp*Ti]CuBr**, the presence of the impurity did not impact the photobehavior [30].

3.2. Structural Characterization

3.2.1. General Structural and Packing Discussion

The four complexes with CuBr coordinated between the alkynes have been characterized by single-crystal X-ray diffraction (Figures 4–7, Tables 1 and 2 and Supplementary Materials Figures S9–S14 and Tables S1 and S2). Structural metrics for **^{Ph}[Cp*Ti]CuBr** have

been previously published [30] and are included in Table 2 for comparison. In general, the structures of the complexes investigated herein are quite similar to a range of arylalkynyltitanocenes with CuBr coordinated between the alkynes [29]. The packing structure and unique features of each structure are discussed below.

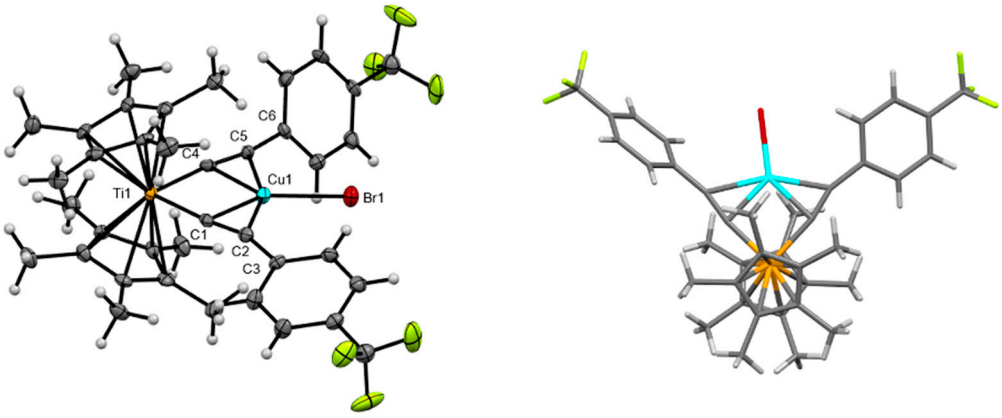

Figure 4. Crystal structure of ^{PhCF3}**[Cp*Ti]CuBr** shown as 50% probability ellipsoids (**left**) and as an overhead wire frame view (**right**). Color code: Ti (orange); Cu (turquoise); Br (red); F (light green).

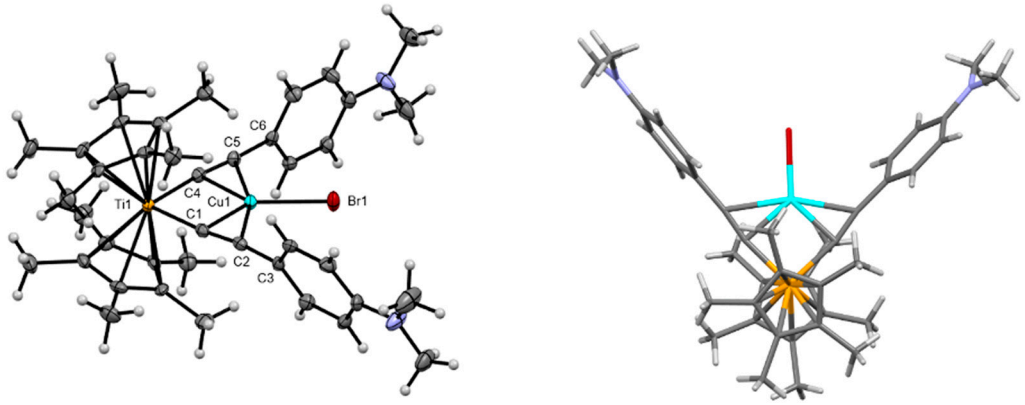

Figure 5. Crystal structure of ^{DMA}**[Cp*Ti]CuBr** shown as 50% probability ellipsoids (**left**) and as an overhead wire frame view (**right**). Color code: Ti (orange); Cu (turquoise), Br (red).

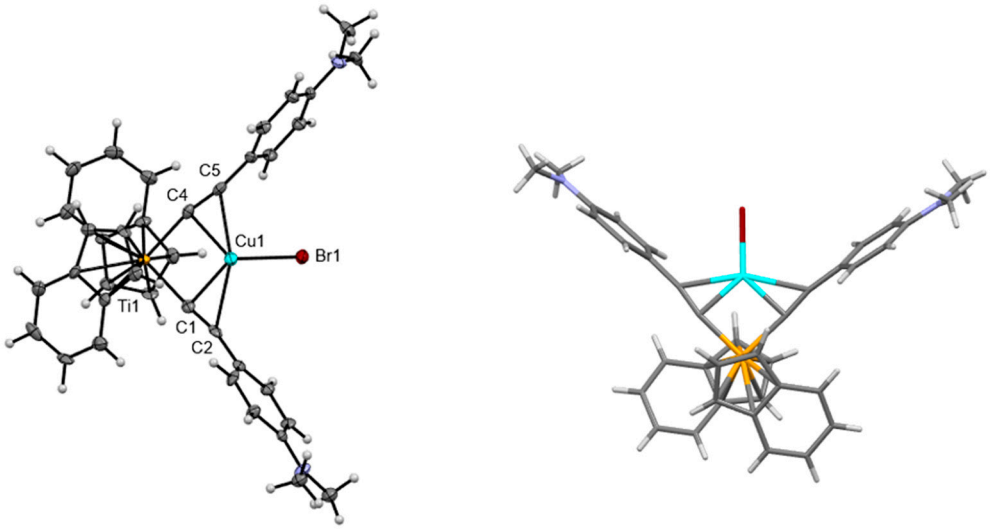

Figure 6. Crystal structure of ^{DMA}**[IndTi]CuBr** shown as 50% probability ellipsoids (**left**) and as an overhead wire frame view (**right**). Color code: Ti (orange); Cu (turquoise); Br (red).

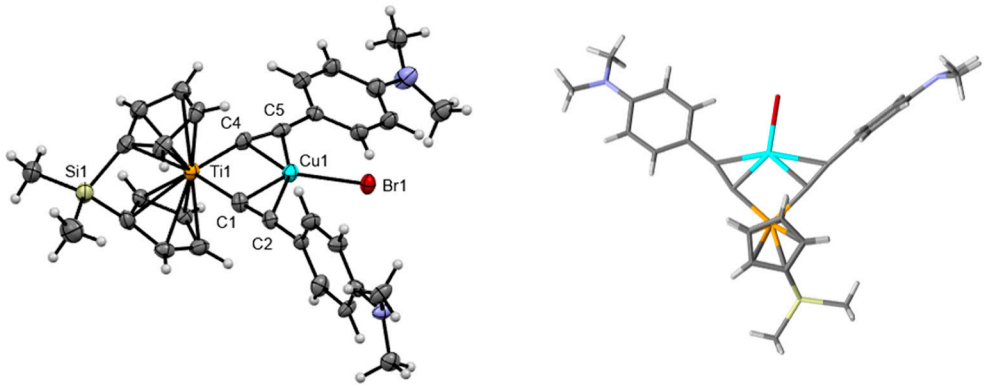

Figure 7. Crystal structure of ^{DMA}**[*ansa*-CpTi]CuBr** shown as 50% probability ellipsoids (**left**) and as an overhead wire frame view (**right**). Color code: Ti (orange); Cu (turquoise); Br (red); Si (yellow).

Table 2. Selected structural metrics.

	^{Ph}[Cp*Ti]CuBr [30]	^{PhCF_3}[Cp*Ti]CuBr	^{DMA}[Cp*Ti]CuBr [a]		^{DMA}[IndTi]CuBr	^{DMA}[*ansa*-CpTi]CuBr
			(1)	(2)		
∠ Cp–Ti–Cp [b]	141.6°	141.23(19)°	141.24(15)°	141.46(15)°	135.7(2)°	131.5(3)°
∠ C1–Ti–C4	88.0(4)°	88.93(16)°	92.89(15)°	91.48(15)°	92.6(2)°	92.5(3)°
∠ Ti–C_αC	172.0(7)°	167.8(4)°, 169.6(4)°	168.8(3)°, 167.5(3)°	167.9(3)°, 169.3(3)°	171.9(5)°, 165.0(5)°	176.6(7)°, 165.3(6)°
∠ C≡C–C	160.1(9)°	158.1(4)°, 165.5 (4)°	173.9(4)°, 170.1(4)°	172.3(4)°, 168.8(4)°	167.3(6)°, 168.1(6)°	172.8(8)°, 162.6(7)°
∠ Ti–Cu–Br	180°	173.77(3)°	176.17(3)°	166.10(3)°	177.07(5)°	168.91(12)°
Ti–Cp [c] (Å)	2.04(2)	2.099(4), 2.095(4)	2.099(4), 2.104(4)	2.104(4), 2.100(4)	2.083(6), 2.072(6)	2.054(7), 2.065(7)
Ti–$C_{C\equiv C}$ (Å)	2.080(8)	2.084(4), 2.093(4)	2.090(4), 2.090(4)	2.085(4), 2.082(4)	2.081(6), 2.081(6)	2.069(8), 2.090(8)
Dihedral [d]	31.1(7)°	64.90(11)°, 19.6(2)°	70.41(11)°, 83.18(12)°	68.42(12)°, 88.12(12)°	84.75(13)°, 78.55(15)°	82.36(18)°, 22.01(12)°
Me/Cp dev [e] (Å)	0.20	0.22	0.20	0.20	-	-

[a] The unit cell contains two unique molecules. Both are included in this column. [b] Angle between the cyclopentadienyl centroids and Ti. [c] Titanium to cyclopentadienyl centroid distance. [d] Dihedral angle between aryl plane and the plane formed by the Ti and the alkynyl carbons. [e] Average deviation of the methyl carbons from the plane of the cyclopentadienyl ring of the Cp* ligand.

The ^{PhCF_3}**[Cp*Ti]CuBr** (Figure 4) complex crystallized as a THF solvate, with one fully unique complex and one THF molecule in the asymmetric unit. The two aryl substituents of ^{PhCF_3}**[Cp*Ti]CuBr** have rotamer orientations quite different from one another, with one much more in plane with the alkyne-Ti-alkyne plane (dihedral angle of 19.6(2)°) than the other (64.90(11)°). The length of the Cu–Br bond is 2.3148(7) Å, which is typical for these complexes [29,30]. The Cu–Br bond is angled slightly away from the in-plane-rotated aryl group (Figure 4, right), perhaps to provide steric accommodation for the in-plane $PhCF_3$ ring. Neighboring complexes display C–H···F short contacts between CF_3 fluorine atoms and Cp* methyl hydrogen atoms and $PhCF_3$ hydrogen atoms. The THF molecules maintain C–H···O contacts to the $PhCF_3$ group that displays more out-of-plane rotation, while also interacting with an additional complex via C–H···Br short contacts. The packing of molecules is shown in the Supplementary Materials, Figure S9.

For ^{DMA}**[Cp*Ti]CuBr** (Figure 5), there are two unique complexes in the asymmetric unit. They display slightly different rotamer orientations of the aryl planes relative to the alkyne-Ti-alkyne plane (Table 2, dihedral angles). A more noticeable distinction between the unique complexes is their different CuBr attachment into the alkynyl pocket—one is mostly in the alkyne-Ti-alkyne plane (Ti–Cu–Br = 176.17(3)°) and the other has the Cu–Br bond

pointing slightly out of plane (Ti–Cu–Br = 166.10(3)°), while both complexes maintain similar Cu–Br distances of 2.2951(6) Å and 2.3203(6) Å (Supplementary Materials Figure S13). The long-range structure features double-stranded chains of complexes propagating along the *b*-axis enabled by C–H···Br contacts originating from the DMA methyl carbon atoms (Supplementary Materials Figure S10). Given the only slightly different dihedral angles of both DMA ligands to the alkyne-Ti-alkyne plane occurring in both unique complexes, it seems the out-of-plane deviation in Cu–Br may be a result of these packing interactions.

The structure of ^{DMA}**[IndTi]CuBr** (Figure 6) has one fully unique complex in the asymmetric unit, and the refinement indicated substitution of 19% of the Br sites as OH in a substitutional disorder (Cu–Br = 2.3011(11) Å). Given that the elemental analysis for this complex is consistent with the CuBr complex, the substitution likely occurs during crystallization. A crystal of a second sample with lower purity (and using different crystal growth conditions) was dominated by OH substitution (71% OH and 29% Br). However, minimal structural perturbation is introduced by Br/OH exchange in this system. Namely, both ^{DMA}**[IndTi]CuBr** samples crystallize in the same space group and effectively have the same lattice parameters (accounting for some contraction in the OH-majority crystal, Supplementary Materials Table S1 and Figure S14). The key bond angles and interatomic distances are also nearly identical for the two samples (Supplementary Materials Table S2). Using the majority-Br-occupied sample as the representative example here, the dihedral angles between the DMA planes and the alkyne-Ti-alkyne plane indicate approximately perpendicular orientations of similar magnitude (84.75(13)° and 78.55(15)°). The packing extends into a three-dimensional framework via multiple C–H···Br short contacts (Supplementary Materials Figure S11).

In the structure of ^{DMA}**[*ansa*-CpTi]CuBr** (Figure 7) there is one fully unique complex in the asymmetric unit, and also a partial substitution of OH for Br in the crystal structure (33% OH and 67% Br; Cu–Br = 2.290(3) Å). Given the lack of variation in the structural metrics upon OH/Br substitution for ^{DMA}**[IndTi]CuBr**, the majority-Br-occupied structure is likely representative of ^{DMA}**[*ansa*-CpTi]CuBr**. Rotations of the DMA ligands in this complex are similar to what occurs in ^{PhCF_3}**[Cp*Ti]CuBr** where one ligand remains mostly in-plane (dihedral angle of 22.01(12)°) and the second ligand is approximately perpendicular (82.36(18)°) relative to the alkyne-Ti-alkyne plane. This again results in CuBr attachment that bends away from the co-planar ligand (Figure 7, right). The bromine atom interacts with three neighboring complexes via C–H···Br short contacts to create a three-dimensional framework. (Supplementary Materials Figure S12).

3.2.2. Comparison of Key Structural Metrics

For all complexes, the arylethynyl ligands linked to Ti create a binding pocket for CuBr. A comparison of the C–Ti–C bond angle for the Cp* and Ind complexes shows that this angle appears dependent on the aryl substituent. Namely, this angle is approximately 88°–89° for the Ph and $PhCF_3$ substituents but increases to approximately 91.5°–93° for the dimethylaniline (DMA) substituent (Table 2). A comparison of the dihedral angle between the aryl planes and the alkyne-Ti-alkyne plane also indicates that complexes with the DMA substituent behave differently (particularly for the Cp* and Ind derivatives—the *ansa*-Cp derivative will be discussed separately below). Namely, for the DMA substituent, this dihedral angle is closer to 90° (the aryl planes being nearly perpendicular to the alkyne-Ti-alkyne plane), whereas for the Ph and $PhCF_3$ substituents, at least one of the two dihedral angles in each molecule is <32° and the largest dihedral angle is only ~65° (Table 2 and Figures 4–7). It is noteworthy that the corresponding Cp complexes without CuBr bound between the alkynes, ^{Ph}**[Ti]** (Figure 1), and ^{DMA}**[Ti]** have been carefully investigated regarding such aryl rotamers. It was found that there was very little barrier

to rotation of the Ph substituent, but a much larger barrier for DMA rotation, and the perpendicular orientation of the DMA substituents was the most thermodynamically favored [49]. The reason given was that conjugation involving the lone pair on the N atom results in a cumulene-like structure, Ti=C=C=C_{aryl}, as one resonance structure. It is possible that because such conjugation involves orbitals on Ti, that the perpendicular orientation is the one that most favors such conjugation. This may also be occurring in the CuBr complexes investigated herein. Such conjugation could also explain the slightly larger C-Ti-C bond angle for the DMA complexes, because electron-electron repulsion from the partial double bond character might slightly increase that angle.

A comparison of the angle formed between the cyclopentadienyl centroids and the central Ti for each complex is also worthwhile. This is because one hypothesis given for the observation that the Cp* complex, **^{Ph}[Cp*Ti]CuBr**, phosphoresces in RT solution (whereas the Cp derivative, **^{Ph}[Ti]CuBr**, does not) was that the steric bulk provided by the Cp* ligand limits excited-state structural rearrangement through steric congestion [30]. Excited-state structural rearrangement is known to increase the rate constant for non-radiative decay, thus competitively diminishing radiative decay and shortening the overall excited-state lifetime [17]. Evidence cited for steric congestion involved the centroid-Ti-centroid angle, which for **^{Ph}[Ti]CuBr** is 134.2°, and for **^{Ph}[Cp*Ti]CuBr** is 141.6°. The expansion of this angle for the Cp* complex was attributed to increased repulsion between the Me substituents on the Cp* ligands [30]. The bond angle is described as being due to a balance between methyl-methyl contacts and contacts between the aryl hydrogens and the same methyl groups. Further evidence cited for such congestion is that the methyl groups on **^{Ph}[Cp*Ti]CuBr** bend away from each other, deviating from the cyclopentadienyl plane by 0.20 Å.

The two Cp* complexes reported herein have nearly identical centroid-Ti-centroid angles to that of **^{Ph}[Cp*Ti]CuBr** (Table 2). Furthermore, the average deviation of the methyl groups from the cyclopentadienyl plane for **^{PhCF_3}[Cp*Ti]CuBr** (0.22 Å) and **^{DMA}[Cp*Ti]CuBr** (0.20 Å) compare well with that of **^{Ph}[Cp*Ti]CuBr** (0.20 Å). As will be shown below, both of these Cp* complexes are emissive in RT fluid solutions. The indenyl complex, **^{DMA}[IndTi]CuBr**, on the other hand, has a centroid-Ti-centroid angle (135.7(2)°) much closer to that of **^{Ph}[Ti]CuBr** and that may indicate that the fused aryl ring on the indenyl complex is better able to avoid congestion through a conformation where the two fused aryl rings are offset, both avoiding each other and avoiding interaction with the arylethynyl ligand. As will be discussed below, **^{DMA}[IndTi]CuBr**, is not emissive in RT fluid solution.

Lastly, for **^{DMA}[*ansa*-CpTi]CuBr**, the centroid-Ti-centroid angle (131.5(3)°) is particularly acute and this likely results from the short $SiMe_2$ bridge between the two cyclopentadienyl rings. Though this bridge likely inhibits rotational movement of the Cp rings, this pinning back of the Cp rings likely minimizes steric congestion between the Cp rings and the arylethynyl substituents. As will be discussed below, **^{DMA}[*ansa*-CpTi]CuBr**, is not emissive in RT fluid solution. One notable difference between **^{DMA}[*ansa*-CpTi]CuBr** and the corresponding Ind and Cp* complexes with C_2DMA ligands is the dihedral angle between the aryl rings and the alkyne-Ti-alkyne plane. Whereas for the **^{DMA}[IndTi]CuBr** and **^{DMA}[Cp*Ti]CuBr** complexes, both aryl rings were nearly perpendicular to the alkyne-Ti-alkyne plane, for **^{DMA}[*ansa*-CpTi]CuBr**, one is close to perpendicular (82.36(18)°) and the other is closer to coplanar (22.01(12)°). It is unclear what causes this difference, but the more acute centroid–Ti–centroid angle due to the $SiMe_2$ bridge for this complex is a likely candidate—and this may result in different packing thermodynamics.

3.3. Photochemical and Photophysical Characterization

3.3.1. Comparison of the Cp* Complexes

As discussed above, the enhanced phosphorescence of ^{Ph}**[Cp*Ti]CuBr** vs. ^{Ph}**[Ti]CuBr** was attributed to increased steric bulk of the Cp* ligand vs. the Cp ligand [30]. However, the excited state character also changed. Though for ^{Ph}**[Ti]CuBr** the lowest-energy CT transition was dominated by CuBr-to-Ti CT and phenylethynyl-to-Ti LMCT, the dominant transitions involved for ^{Ph}**[Cp*Ti]CuBr** changed to Cp*-to-Ti LMCT and CuBr-to-Ti CT, with very little phenylethynyl-to-Ti LMCT. Perhaps the greater emission for ^{Ph}**[Cp*Ti]CuBr** can be attributed to the presence of Cp*-to-Ti LMCT orbital character in the excited state. To test this, we have prepared the corresponding Cp* complex with an ethynyldimethylaniline (C_2DMA) ligand, ^{DMA}**[Cp*Ti]CuBr**. We hypothesize that the more electron-rich DMA substituent (compared to phenyl) will lead to increased arylethynyl-to-Ti LMCT character. Furthermore, we have also prepared a complex with a more electron-deficient substituent than phenyl, namely ^{PhCF_3}**[Cp*Ti]CuBr**, that we hypothesize will be dominated by Cp*-to-Ti LMCT due to the electron-poor nature of the arylethynyl ligand.

^{DMA}**[Cp*Ti]CuBr** is phosphorescent both in 77 K 2-methyltetrahydrofuran (2-Me-THF) glass and in fluid solution at RT (Figure 8). The observation that the excitation spectra are a good match with the absorbance spectrum is a good indication that emission originates from the analyte rather than an impurity (Supplementary Materials Figure S15). As is typical for these complexes [29], the 77 K emission spectrum of the CuBr coordinated complex is red-shifted compared to the parent ^{DMA}**[Cp*Ti]** (Supplementary Materials, Figure S16). The photoluminescent quantum yield for ^{DMA}**[Cp*Ti]CuBr** ($\Phi_{PL} = 3.7 \times 10^{-3}$) and the phosphorescence lifetime ($\tau = 0.16$ µs) compare favorably with the corresponding phenyl complex, ^{Ph}**[Cp*Ti]CuBr** (Table 3).

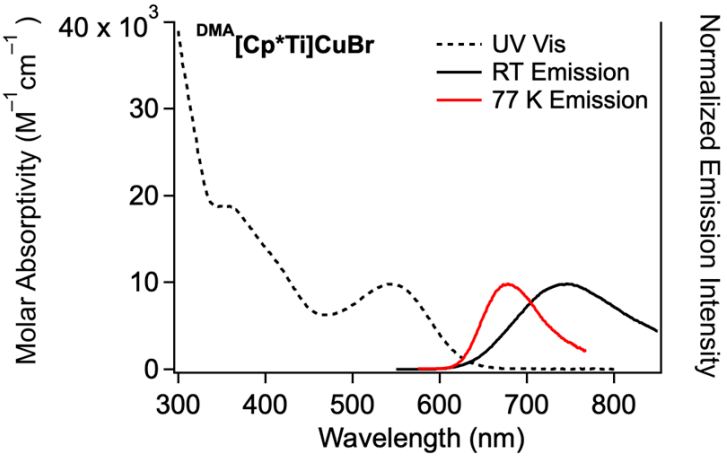

Figure 8. Absorption spectrum of ^{DMA}**[Cp*Ti]CuBr** in RT THF, and emission spectra in RT THF solution (λ_{ex} = 365 nm) and 77 K 2-MeTHF glass (λ_{ex} = 360 nm).

Table 3. Photophysical Data for a Series of ^{R}**[Cp*Ti]CuBr** complexes.

	λ_{max} 77 K	τ 77 K (µs)	λ_{max} RT	τ RT (µs)	Φ_{PL} RT [a]
^{DMA}**[Cp*Ti]CuBr**	679 nm	124 [b]	744 nm	0.16 [c]	3.7×10^{-3}
^{Ph}**[Cp*Ti]CuBr** [d]	619 nm	655	693 nm	0.18	1.3×10^{-3}
^{PhCF3}**[Cp*Ti]CuBr**	629 nm	1130 [b]	635 nm	– [e]	4.5×10^{-4}

[a] Values reported in air-saturated solution and appear independent to the presence of O_2 (i.e., insensitive to purging with Ar). [b] Weighted average from double-exponential fit of the emission decay trace (Supplementary Materials Figure S17). Weighted average performed according to [52]. [c] Lifetime obtained from single-exponential fit of the emission decay trace (Supplementary Materials Figure S18). [d] Data from [30,31]. [e] Below detection limits of our instrument (<120 ns).

To further investigate the orbital involvement in this emissive excited state, density functional theory (DFT) and time-dependent DFT (TDDFT) were performed using B3LYP/6-311+G(d) functional that was shown to effectively model the excited-state behavior of **^{Ph}[Cp*Ti]CuBr** and **^{xyl}[Cp*Ti]CuBr** [31]. Mulliken population analysis was also performed to estimate the charge distribution and quantity of charge transfer for the one-electron transitions of interest (Table 4). The lowest-energy triplet excited state for **^{DMA}[Cp*Ti]CuBr** is 93% HOMO-to-LUMO in character, being dominated by C_2DMA-to-Ti LMCT (Figure 9, Table 4) with no Cp*-to-Ti LMCT character. This suggests that the presence of Cp*-to-Ti LMCT character is not a prerequisite for the increased lifetime observed in these complexes.

Table 4. Orbital contribution and population analysis for lowest-energy triplet states [a].

Complex (% HOMO-LUMO)	λ(nm) [b]	Ti	Cp*	C_2Aryl	CuBr
^{DMA}[Cp*Ti]CuBr (93%)	687	1 → 49 (48)	3 → 8 (5)	83 → 38 (−45)	14 → 5 (−9)
^{Ph}[Cp*Ti]CuBr [c] (80%)	577	3 → 50 (47)	27 → 8 (−19)	39 → 35 (−4)	31 → 7 (−24)
^{PhCF3}[Cp*Ti]CuBr (88%)	591	10 → 49 (39)	56 → 8 (−48)	26 → 34 (8)	8 → 8 (0)

[a] Mulliken population analysis was performed using GaussSum 3.0 [35]. The numbers in parentheses in the body of the table indicate the increase or decrease in electron density due to the one-electron transition. Positive numbers indicate an increase, and negative numbers indicate a decrease. [b] TDDFT predicted wavelength of the lowest-energy triplet state. [c] Data from [31] included for comparison.

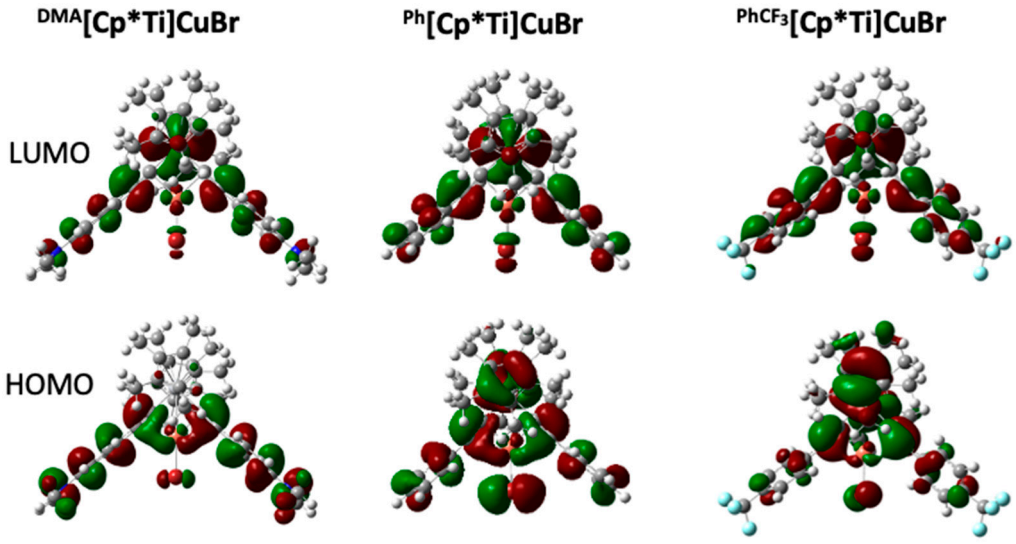

Figure 9. Frontier orbitals (isovalue = 0.02) for **^{DMA}[Cp*Ti]CuBr**, **^{Ph}[Cp*Ti]CuBr**, and **^{PhCF_3}[Cp*Ti]CuBr**. The data for **^{Ph}[Cp*Ti]CuBr** is from [31].

^{PhCF3}[Cp*Ti]CuBr also phosphoresces in both 77 K 2-Me-THF glass and in RT fluid solution (Figure 10). Again, the observation that the excitation spectra are a good match with the absorbance spectrum is a good indication that emission originates from the analyte rather than an impurity (Supplementary Materials, Figure S19). It is noteworthy that the RT solution phosphorescence quantum yield and lifetime are significantly smaller than those for **^{Ph}[Cp*Ti]CuBr** and **^{DMA}[Cp*Ti]CuBr** (Table 3). Furthermore, whereas the coordination of CuBr consistently results in a redshift in the emission band of >1600 cm^{-1} relative to the parent complex [29], for **^{PhCF_3}[Cp*Ti]CuBr**, there is a blueshift of 400 cm^{-1} (Supplementary Materials, Figure S20). In addition, coordination of CuBr typically results in emission lifetimes at 77 K in the μs range [29]. However, the excited-state lifetime for **^{PhCF3}[Cp*Ti]CuBr** is in the ms range (Table 3). To further investigate the excited-state behavior, DFT and TDDFT were performed using B3LYP/6-311+G(d) functional employed for **^{DMA}[Cp*Ti]CuBr**. For this complex, the HOMO has very little electron density on the

C_2PhCF_3 ligand and the transition is mainly Cp*-to-Ti LMCT and includes a small amount of Cp*-to-C_2PhCF_3 ligand-to-ligand CT (LL'CT) (Figure 9, Table 4). Thus, the CT transition does not appear to involve Cu and this may lower the degree of spin–orbit coupling induced by the heavier Cu atom, resulting in longer phosphorescence lifetimes at 77 K due to decreased rate constants for triplet to singlet transitions. It is also likely that diminished spin–orbit coupling decreases the rate of intersystem crossing (ISC) to the emissive triplet state so that in RT solution, direct nonradiative decay from the initially formed singlet is competitive with ISC, and this would diminish the overall phosphorescence quantum yield and lifetime. It is also worth noting that the charge-transfer components for all complexes only account for about half of the overall one-electron transition, with the remainder largely being of π-to-π* character localized on the arylethynyl ligand (Table 4).

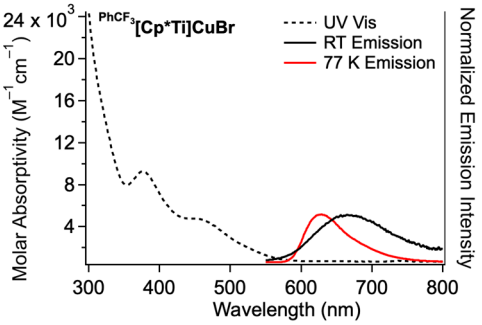

Figure 10. Absorption spectrum of **^{PhCF_3}[Cp*Ti]CuBr** in RT THF, and emission spectra in RT THF solution (λ_{ex} = 450 nm) and 77 K 2-Me-THF glass (λ_{ex} = 377 nm).

3.3.2. Replacing Cp* with Indenyl or *ansa*-Cp

Previous research on this class of titanocenes has suggested that steric constraint can be used to increase the lifetimes of the emissive excited state [30,31]. It is important to recognize the rationale for why steric constraint might improve these lifetimes. In fluid solution, the lowest-energy triplet excited state (T_1) for a flexible molecule will necessarily undergo geometric rearrangement relative to the ground state (S_0). Thus, the T_1 potential well is shifted along the nuclear coordinate (relative to S_0) setting up a low barrier for nonradiative decay via T_1 to S_0 potential well surface crossing (Figure 11). A rigid molecule will not undergo the same degree of geometric rearrangement and thus the T_1 potential well will be more "nested" with the ground state potential well, increasing the barrier for nonradiative decay through surface crossing. This should increase the overall excited-state lifetime.

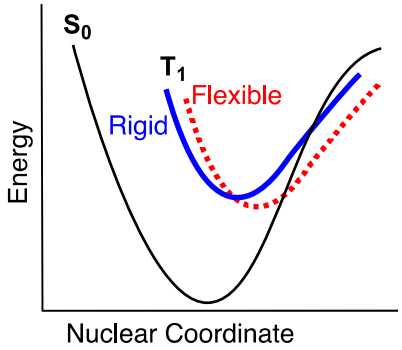

Figure 11. Potential-well diagram for a system with a singlet (S_0) ground state and a triplet (T_1) excited state shown for both a flexible geometry (red dashed line), and a rigid geometry (blue).

Given that the Cp* complex with the DMA ligand is luminescent in solution at RT, it is reasonable to study other forms of steric bulk and constraint at the Cp ligand. We chose

to prepare both the ^{DMA}**[IndTi]CuBr** and ^{DMA}**[*ansa*-CpTi]CuBr** complexes (Figure 2) to compare directly to ^{DMA}**[Cp*Ti]CuBr**. The indenyl ligand was chosen because the increased steric bulk compared to cyclopentadienyl might have a similar effect as the Cp* ligand. The *ansa*-Cp ligand was chosen because of the constraint imposed by the Me_2Si bridge between the two Cp ligands. Yet as discussed in the structural discussion, there was evidence that neither of these ligands resulted in the same degree of steric congestion that the Cp* ligand provided. Thus, it is perhaps unsurprising that neither of these complexes showed emission in RT THF solution. However, both ^{DMA}**[*ansa*-CpTi]CuBr** and ^{DMA}**[IndTi]CuBr** are emissive in 77 K 2-Me-THF glass (Figure 12). Again, the excitation spectra are a good match with the absorption spectra (Supplementary Materials, Figures S21 and S23). Upon coordination of CuBr, there is a significant redshift in the emission relative to the corresponding parent complexes as is common for this class of compounds (Table 5 and Supplementary Materials, Figures S22 and S24).

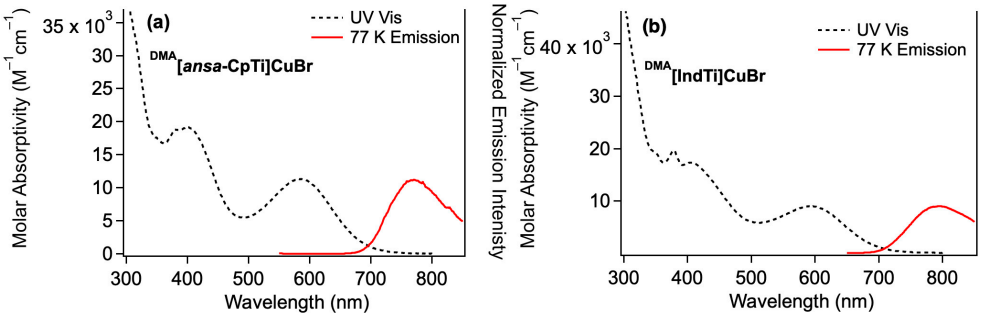

Figure 12. (**a**) ^{DMA}**[*ansa*-CpTi]CuBr** UV-Vis spectrum in RT THF solution, and emission spectrum in 77 K 2-MeTHF glass (λ_{ex} = 400 nm). (**b**) ^{DMA}**[IndTi]CuBr** UV-Vis spectrum in RT THF solution, and emission spectrum in 77 K 2-MeTHF glass (λ_{ex} = 550 nm).

Table 5. Effect of CuBr coordination on photostability.

	Parent		CuBr Complex	
	λ_{max} 77 K	Φ_{decomp} RT [a]	λ_{max} 77 K	Φ_{decomp} RT [a]
^{DMA}**[*ansa*-CpTi]**	675 nm	0.15	770 nm	$<1 \times 10^{-4}$
^{DMA}**[IndTi]**	705 nm	0.24	793 nm	3.6×10^{-4}
^{DMA}**[Cp*Ti]**	633 nm	0.36	679 nm	5.1×10^{-4}
^{PhCF3}**[Cp*Ti]**	644 nm	0.48	626 nm	6.1×10^{-3}

[a] Measurement appears independent to conditions of air-saturation vs. Ar-saturation.

It is worthwhile to note that the 77 K emission maximum for both ^{DMA}**[*ansa*-CpTi]CuBr** (770 nm) and ^{DMA}**[IndTi]CuBr** (793 nm) are significantly redshifted relative to the 77 K emission maxima for the three Cp* compounds that show phosphorescence in RT fluid solution, namely ^{DMA}**[Cp*Ti]CuBr** (679 nm), ^{Ph}**[Cp*Ti]CuBr** (619 nm), and ^{xyl}**[Cp*Ti]CuBr** (692 nm). Note that if the T_1 potential well is lowered in energy (Figure 11), this would also reduce the activation barrier for T_1 to S_0 potential well surface crossing. Furthermore, lowering the energy of the T_1 state may also increase the rate of nonradiative decay through energy-gap law behavior [53]. Thus, the lack of RT emission from either ^{DMA}**[*ansa*-CpTi]CuBr** or ^{DMA}**[IndTi]CuBr** cannot be attributed unequivocally to the *ansa*-Cp ligand and the indenyl ligand not providing sufficient steric constraint.

3.3.3. Impact of CuBr Coordination on Photostability

Previous reports on arylethynyltitanocenes have demonstrated that coordination of CuBr both redshifts the emission and decreases the quantum yield for photodecomposition, Φ_{decomp}. For a series of homoleptic cyclopentadienyl complexes where only the aryl substituent and the metal halide bound between the alkynes were varied, the data was

explained using a mechanism where photodecomposition occurred out of the lowest energy triplet excited state, and that the decomposition rate constant was dependent on the energy of the excited state [29]. This hypothesis can be explained by the assumption that decomposition requires breaking Ti-C bonds and thus there is a threshold of excited-state energy necessary. Largely, the data presented here are consistent with that hypothesis. For example, for ^{DMA}**[*ansa*-CpTi]**, ^{DMA}**[IndTi]**, and ^{DMA}**[Cp*Ti]** there is a significant redshift in the 77 K emission upon coordination of CuBr and a concomitant lowering of Φ_{decomp} (Table 5). The one complex that deviates from this trend is ^{PhCF3}**[Cp*Ti]CuBr**, which as discussed earlier, shows a blue-shift in the emission relative to the parent ^{PhCF3}**[Cp*Ti]**. Yet there is still a lowering of Φ_{decomp}. One possible explanation is that this complex is the first for which the excited state does not involve charge transfer to Ti from either CuBr or the arylethynyl ligand—and thus the decomposition mechanism may differ from that proposed for previously investigated complexes [29].

4. Conclusions

Several different methods of providing steric constraint to arylethynyltitanocenes as a means to increase the excited-state lifetimes were investigated. Chiefly, comparison was made between complexes of three different cyclopentadienyl analogs, Cp*, Ind, and *ansa*-Cp. Whereas ^{DMA}**[Cp*Ti]CuBr** is emissive in RT fluid solution, neither ^{DMA}**[IndTi]CuBr**, nor ^{DMA}**[*ansa*-CpTi]CuBr** are emissive under those conditions. The structures of the complexes suggest that the Cp* complex shows significant steric congestion involving Me-Me contacts between the Cp* ligands and contacts between the Me groups and the aryl ring of the arylethynyl ligand. Similar steric constraint does not appear to exist for the corresponding Ind and *ansa*-Cp complexes. Furthermore, the fact that the *ansa*-Cp derivative is not emissive suggests that simply hindering rotational motion of the Cp ligands does not provide sufficient constraint to result in emission. However, it was also noted that both ^{DMA}**[IndTi]CuBr** and ^{DMA}**[*ansa*-CpTi]CuBr** have lower-energy excited states than ^{DMA}**[Cp*Ti]CuBr**, so the lack of emission cannot be unequivocally attributed to a lack of steric constraint. Additionally, the relationship between the orbital character of the excited state and the observation of emission in RT fluid solution was examined. It does not appear that Cp*-to-Ti LMCT character is required for such behavior. However, the results suggest that the coordinated CuBr plays a role in spin–orbit coupling, enhancing the rates of intersystem crossing from the initially formed singlet state to the phosphorescent triplet state and radiative decay from that triplet state. Such a role for coordinated CuX (X = Br, Cl) has been proposed previously for structurally similar ethynylferrocene (C_2Fc) complexes, $Cp_2Ti(C_2Fc)_2CuX$ [54].

Supplementary Materials: The following supporting information can be downloaded at https://www.mdpi.com/article/10.3390/cryst15080745/s1, Figures S1–S7: ^{1}H NMR spectra, Figure S8: Infrared spectra, Figures S9–S12: Crystal packing diagrams for crystallographically characterized complexes, Figure S13: Diagrams of two unique molecules for ^{DMA}**[Cp*Ti]CuBr** unit cell, Table S1: Crystallographic data and refinement details for ^{DMA}**[IndTi]CuBr$_{0.29}$(OH)$_{0.71}$**, Figure S14: Crystal structure of ^{DMA}**[IndTi]CuBr$_{0.29}$(OH)$_{0.71}$**, Table S2: Structural metrics for ^{DMA}**[IndTi]CuBr$_{0.29}$(OH)$_{0.71}$**, Figure S15: Absorption and, RT and 77 K excitation spectra for ^{DMA}**[Cp*Ti]** and ^{DMA}**[Cp*Ti]CuBr**, Figure S16: 77 K emission spectra for ^{DMA}**[Cp*Ti]** and ^{DMA}**[Cp*Ti]CuBr**, Figure S17: Luminescence decay trace for ^{DMA}**[Cp*Ti]CuBr** and ^{PhCF3}**[Cp*Ti]CuBr** in 77 K 2-MeTHF, Figure S18: Luminescence decay trace for ^{DMA}**[Cp*Ti]CuBr** in THF solution, Figure S19: Absorption and, RT and 77 K excitation spectra for ^{PhCF3}**[Cp*Ti]** and ^{PhCF3}**[Cp*Ti]CuBr**, Figure S20: 77 K emission spectra for ^{PhCF3}**[Cp*Ti]** and ^{PhCF3}**[Cp*Ti]CuBr**, Figure S21: Absorption and, RT and 77 K excitation spectra for ^{DMA}**[*ansa*-CpTi]** and ^{DMA}**[*ansa* CpTi]CuBr**, Figure S22: 77 K emission spectra for ^{DMA}**[*ansa*-CpTi]** and ^{DMA}**[*ansa*-CpTi]CuBr**, Figure S23: Absorption and, RT and 77 K excitation

spectra for ^{DMA}**[IndTi]** and ^{DMA}**[IndTi]CuBr**, Figure S24: 77 K emission spectra for ^{DMA}**[IndTi]** and ^{DMA}**[IndTi]CuBr**.

Author Contributions: Conceptualization, P.S.W.; methodology, M.B., C.D.M. and P.S.W.; validation, M.B., S.C.W., E.A.M., J.H.Z. and C.D.M.; formal analysis, M.B., S.C.W., E.A.M., J.H.Z., R.S.G. and C.D.M.; investigation, M.B., S.C.W., E.A.M., J.H.Z., R.S.G., J.S.M. and C.D.M.; resources, P.S.W. and C.D.M.; data curation, M.B., C.D.M. and P.S.W.; writing—original draft preparation, M.B., S.C.W., E.A.M., R.S.G., C.D.M. and P.S.W.; writing—review and editing, M.B., S.C.W., E.A.M., J.H.Z., R.S.G., J.S.M., C.D.M. and P.S.W.; visualization, M.B., S.C.W., E.A.M., J.H.Z. and C.D.M.; supervision, P.S.W.; project administration, P.S.W.; funding acquisition, P.S.W. and C.D.M. All authors have read and agreed to the published version of the manuscript.

Funding: Support is acknowledged from the National Science Foundation under Grant No. 2055326. Any opinions, findings and conclusions or recommendations expressed in this material are those of the authors and do not necessarily reflect those of the National Science Foundation.

Data Availability Statement: CCDC 2475385-2475389 contain the supplementary crystallographic data for this paper. These data can be obtained from the CCDC, 12 Union Road, Cambridge CB2 1EZ, UK; Fax: +44-1223-336033.

Acknowledgments: The authors thank George C. Shields for providing computational infrastructure [55], in part through a Research Corporation for Science Advancement Cottrell Instrumentation Supplements Award #27446.

Conflicts of Interest: The authors declare no conflicts of interest. The funders had no role in the design of the study; in the collection, analyses, or interpretation of data; in the writing of the manuscript; or in the decision to publish the results.

Abbreviations

The following abbreviations are used in this manuscript:

2-Me-THF	2-methyltetrahydrofuran
ansa-Cp	$Me_2Si(\eta^5\text{-}C_5H_4)_2$
Cp	Cyclopentadienyl
Cp*	Pentamethylcyclopentadienyl
DMA	Dimethylaniline
Φ_{decomp}	Quantum yield for photodecomposition
Φ_{PL}	Quantum yield for photoluminescence
Ind	Indenyl
LL'CT	Ligand-to-ligand charge transfer
LMCT	Ligand-to-metal charge transfer
MC	Metal-centered
MXMCT	Metal halide-to-metal charge transfer
RT	Room temperature

References

1. Yamazaki, Y.; Takeda, H.; Ishitani, O. Photocatalytic reduction of CO_2 using metal complexes. *J. Photochem. Photobiol. C Photochem. Rev.* **2015**, *25*, 106–137. [CrossRef]
2. Brennaman, M.K.; Dillon, R.J.; Alibabaei, L.; Gish, M.K.; Dares, C.J.; Ashford, D.L.; House, R.L.; Meyer, G.J.; Papanikolas, J.M.; Meyer, T.J. Finding the Way to Solar Fuels with Dye-Sensitized Photoelectrosynthesis Cells. *J. Am. Chem. Soc.* **2016**, *138*, 13085–13102. [CrossRef]
3. Zhang, X.; Yamauchi, K.; Sakai, K. Earth-Abundant Photocatalytic CO_2 Reduction by Multielectron Chargeable Cobalt Porphyrin Catalysts: High CO/H_2 Selectivity in Water Based on Phase Mismatch in Frontier MO Association. *ACS Catal.* **2021**, *11*, 10436–10449. [CrossRef]
4. Hedstrand, D.M.; Kruizinga, W.H.; Kellogg, R.M. Light induced and dye accelerated reduction of phenacyl onium salts by 1,4-dihydropyridines. *Tetrahedron Lett.* **1978**, *19*, 1255–1258. [CrossRef]
5. Stephenson, C.; Yoon, T. Enabling Chemical Synthesis with Visible Light. *Acc. Chem. Res.* **2016**, *49*, 2059–2060. [CrossRef]

6. Marzo, L.; Pagire, S.K.; Reiser, O.; Konig, B. Visible-Light Photocatalysis: Does It make a Difference in Organic Synthesis? *Angew. Chem. Int. Ed.* **2018**, *57*, 10034–10072. [CrossRef] [PubMed]
7. Glaser, F.; Wenger, O.S. Recent progress in the development of transition-metal based photoredox catalysts. *Coord. Chem. Rev.* **2020**, *405*, 213129. [CrossRef]
8. Chan, A.Y.; Perry, I.B.; Bissonnette, N.B.; Buksh, B.F.; Edwards, G.A.; Frye, L.I.; Garry, O.L.; Lavagnino, M.N.; Li, B.X.; Liang, Y.; et al. Metallaphotoredox: The Merger of Photoredox and Transition Metal Catalysis. *Chem. Rev.* **2022**, *122*, 1485–1542. [CrossRef] [PubMed]
9. O'Regan, B.C.; Grätzel, M. A low-cost, high-efficiency solar cell based on dye-sensitized colloidal TiO_2 films. *Nature* **1991**, *353*, 737–740. [CrossRef]
10. Kalyanasundaram, K.; Grätzel, M. Applications of Functionalized Transition Metal Complexes in Photonic and Optoelectronic Devices. *Coord. Chem. Rev.* **1998**, *177*, 347–414. [CrossRef]
11. Housecraft, C.E.; Constable, E.C. Solar energy conversion using first row d-block metal coordination compound sensitizers and redox mediators. *Chem. Sci.* **2022**, *13*, 1225–1262. [CrossRef] [PubMed]
12. Singh-Rachford, T.N.; Castellano, F.N. Photon upconversion based on sensitized triplet-triplet annihilation. *Coord. Chem. Rev.* **2010**, *254*, 2560–2573. [CrossRef]
13. Zeng, L.; Huang, L.; Han, J.; Han, G. Enhancing Triplet—Triplet Annihilation Upconversion: From Molecular Design to Present Applications. *Acc. Chem. Res.* **2022**, *55*, 2604–2615. [CrossRef]
14. DeRosa, M.C.; Crutchley, R.J. Photosensitized singlet oxygen and its applications. *Coord. Chem. Rev.* **2002**, *233–234*, 351–371. [CrossRef]
15. Ford, P.C.; van Eldik, R. (Eds.) *Photochemistry and Photophysics of Earth-Abundant Transition-Metal Complexes*; Advances in Inorganic Chemistry; Elsevier: Amsterdam, The Netherlands, 2024; Volume 83.
16. Wegeberg, C.; Wenger, O. Luminescent First-Row Transition Metal Complexes. *J. Am. Chem. Soc. Au* **2021**, *1*, 1860–1876. [CrossRef]
17. Morselli, G.; Rebeer, C.; Wenger, O.S. Molecular Design Principles for Photoactive Transition Metal Complexes: A Guide for "Photo-Motivated" Chemists. *J. Am. Chem. Soc.* **2025**, *147*, 11608–11624. [CrossRef] [PubMed]
18. Förster, C.; Heinze, K. Photophysics and photochemistry with Earth-abundant metals—Fundamentals and concepts. *Chem. Soc. Rev.* **2020**, *49*, 1057–1070. [CrossRef]
19. Giobbio, G.; Costa, R.D.; Gaillard, S. Earth-abundant transition metal complexes in light-emitting electrochemical cells: Successes, challenges and perspectives. *Dalton. Trans.* **2025**, *54*, 3573–3580. [CrossRef]
20. Wagenknecht, P.S.; Ford, P.C. Metal Centered Ligand Field Excited States: Their Roles in the Design and Performance of Transition Metal Based Photochemical Molecular Devices. *Coord. Chem. Rev.* **2011**, *255*, 591–616. [CrossRef]
21. Wagenknecht, P.S. Ligand-to-metal charge-transfer states in emissive d^0 metallocenes: Design strategies for titanocene based photocatalysts. In *Photochemistry and Photophysics of Earth-Abundant Transition-Metal Complexes*; Ford, P.C., van Eldik, R., Eds.; Advances in Inorganic Chemistry; Elsevier: Amsterdam, The Netherlands, 2024; Volume 83, pp. 63–109. [CrossRef]
22. Zhang, Y.; Petersen, J.L.; Milsmann, C. A Luminescent Zirconium(IV) Complex as a Molecular Photosensitizer for Visible Light Photoredox Catalysis. *J. Am. Chem. Soc.* **2016**, *138*, 13115–13118. [CrossRef] [PubMed]
23. Zhang, Y.; Lee, T.S.; Favale, J.M.; Leary, D.C.; Petersen, J.L.; Scholes, G.D.; Castellano, F.N.; Milsmann, C. Delayed fluorescence from a zirconium(IV) photosensitizer with ligand-to-metal charge-transfer excited states. *Nat. Chem.* **2020**, *12*, 345–352. [CrossRef]
24. Yang, M.; Sheykhi, S.; Zhang, Y.; Milsmann, C.; Castellano, F.N. Low power threshold photochemical upconversion using a zirconium(IV) LMCT photosensitizer. *Chem. Sci.* **2021**, *12*, 9069–9077. [CrossRef]
25. Urbán, B.; Dunlop, D.; Gyepes, R.; Kubát, P.; Lang, K.; Horáček, M.; Pinkas, J.; Šimková, L.; Lamač, M. Luminescent Zirconocene Complexes with Pendant Phosphine Chalcogenide Donor Groups. *Organometallics* **2023**, *42*, 1373–1385. [CrossRef]
26. Dunlop, D.; Večeřa, M.; Gyepes, R.; Kubát, P.; Lang, K.; Horáček, M.; Pinkas, J.; Šimková, L.; Liška, A.; Lamač, M. Luminescent Cationic Group 4 Metallocene Complexes Stabilized by Pendant N-Donor Groups. *Inorg. Chem.* **2021**, *60*, 7315–7328. [CrossRef] [PubMed]
27. Lamač, M.; Dunlop, D.; Lang, K.; Kubát, P. Group 4 metallocene derivatives as a new class of singlet oxygen photo- sensitizers. *J. Photochem. Photobiol. A Chem.* **2022**, *424*, 113619. [CrossRef]
28. Romain, C.; Choua, S.; Collin, J.-P.; Heinrich, M.; Bailly, C.; Karmazin-Brelot, L.; Bellemin-Laponnaz, S.; Dagorne, S. Redox and Luminescent Properties of Robust and Air-Stable N-Heterocyclic Carbene Group 4 Metal Complexes. *Inorg. Chem.* **2014**, *53*, 7371–7376. [CrossRef]
29. London, H.C.; Pritchett, D.Y.; Pienkos, J.A.; McMillen, C.D.; Whittemore, T.J.; Bready, C.J.; Myers, A.R.; Vieira, N.C.; Harold, S.; Shields, G.C.; et al. Photochemistry and Photophysics of Charge-Transfer Excited States in Emissive d^{10}/d^0Heterobimetallic Titanocene Tweezer Complexes. *Inorg. Chem.* **2022**, *61*, 10986–10998. [CrossRef] [PubMed]
30. Barker, M.; Whittemore, T.J.; London, H.C.; Sledesky, J.M.; Harris, E.A.; Smith Pellizzeri, T.M.; McMillen, C.D.; Wagenknecht, P.S. Design Strategies for Luminescent Titanocenes: Improving the Photoluminescence and Photostability of Arylethynyltitanocenes. *Inorg. Chem.* **2023**, *62*, 17870–17882. [CrossRef]

31. Sledesky, J.M.; Zimmerman, J.H.; London, H.C.; Lambert, E.C.; McMillen, C.D.; Barker, M.; Hanson, K.; Wagenknecht, P.S. Xylylethynyl titanocene with a microsecond emission lifetime photosensitizes singlet-oxygen formation and photon upconversion. *Inorg. Chem.* **2025**, *64*, 14977–14988. [CrossRef]
32. Suzuki, K.; Kobayashi, A.; Kaneko, S.; Takehira, K.; Yoshihara, T.; Ishida, H.; Shiina, Y.; Oishic, S.; Tobita, S. Reevaluation of absolute luminescence quantum yields of standard solutions using a spectrometer with an integrating sphere and a back-thinned CCD detector. *Phys. Chem. Chem. Phys.* **2009**, *11*, 9850–9860. [CrossRef]
33. Frisch, M.J.; Trucks, G.W.; Schlegel, H.B.; Scuseria, G.E.; Robb, M.A.; Cheeseman, J.R.; Scalmani, G.; Barone, V.; Petersson, G.A.; Nakatsuji, H.; et al. *Gaussian 16*; Revision, C.01; Gaussian, Inc.: Wallingford, CT, USA, 2016.
34. Dennington, R.; Keith, T.A.; Millam, J.M. *GaussView*, version 6; Semichem Inc.: Shawnee Mission, KS, USA, 2016.
35. O'Boyle, N.M.; Tenderholt, A.L.; Langner, K.M. cclib: A library for package-independent computational chemistry algorithms. *J. Comp. Chem.* **2008**, *29*, 839–845. [CrossRef]
36. Becke, A.D. Density-functional exchange-energy approximation with correct asymptotic behavior. *Phys. Rev. A At. Mol. Opt. Phys.* **1988**, *38*, 3098–3100. [CrossRef]
37. Lee, C.; Yang, W.; Parr, R.G. Development of the Colle-Salvetti correlation-energy formula into a functional of the electron density. *Phys. Rev. B Condens. Matter Mater. Phys.* **1988**, *37*, 785–789. [CrossRef]
38. McLean, A.D.; Chandler, G.S. Contracted Gaussian-basis sets for molecular calculations. 1. 2nd row atoms, Z = 11−18. *J. Chem. Phys.* **1980**, *72*, 5639–5648. [CrossRef]
39. Wachters, A.J.H. Gaussian basis set for molecular wavefunctions containing third-row atoms. *J. Chem. Phys.* **1970**, *52*, 1033–1036. [CrossRef]
40. Hay, P.J. Gaussian basis sets for molecular calculations-representation of 3d orbitals in transition-metal atoms. *J. Chem. Phys.* **1977**, *66*, 4377–4384. [CrossRef]
41. Clark, T.; Chandrasekhar, J.; Spitznagel, G.W.; Schleyer, P.V.R. Efficient diffuse function-augmented basis-sets for anion calculations. 3. The 3- 21+G basis set for 1st-row elements, Li-F. *J. Comput. Chem.* **1983**, *4*, 294–301. [CrossRef]
42. Frisch, M.J.; Pople, J.A.; Binkley, J.S. Self-Consistent Molecular Orbital Methods. 25. Supplementary Functions for Gaussian Basis Sets. *J. Chem. Phys.* **1984**, *80*, 3265–3269. [CrossRef]
43. Tomasi, J.; Mennucci, B.; Cammi, R. Quantum Mechanical Continuum Solvation Models. *Chem. Rev.* **2005**, *105*, 2999–3093. [CrossRef]
44. *APEX 4*, version 2022.10-0; Bruker-AXS Inc.: Madison, WI, USA, 2022.
45. Sheldrick, G.M. SHELXT—Integrated space-group and crystal-structure determination. *Acta Crystallogr. Sect. A Found. Adv.* **2015**, *71*, 3–8. [CrossRef] [PubMed]
46. Sheldrick, G.M. Crystal structure refinement with SHELXL. *Acta Crystallogr. Sect. C Struct. Chem.* **2015**, *71*, 3–8. [CrossRef]
47. Pinkas, J.; Kubista, J.; Horacek, M.; Mach, K.; Varga, V.; Gyepes, R. Low-valent ansa-dimethylsilylene-, dimethylmethylene-bis(cyclopentadienyl) titanium compounds and ansa-titanium-magnesium complexes. *J. Organomet. Chem.* **2019**, *889*, 15–26. [CrossRef]
48. Pienkos, J.A.; Agakidou, A.D.; Trindle, C.O.; Herwald, D.W.; Altun, Z.; Wagenknecht, P.S. Titanocene as a New Acceptor (A) for Arylamine Donors (D) in D-π-A Chromophores. *Organometallics* **2016**, *35*, 2575–2578. [CrossRef]
49. London, H.C.; Whittemore, T.J.; Gale, A.G.; McMillen, C.D.; Pritchett, D.Y.; Myers, A.R.; Thomas, H.D.; Shields, G.C.; Wagenknecht, P.S. Ligand-to-Metal Charge-Transfer Photophysics and Photochemistry of Emissive d^0 Titanocenes: A Spectroscopic and Computational Investigation. *Inorg. Chem.* **2021**, *60*, 14399–14409. [CrossRef] [PubMed]
50. Lang, H.; Köhler, K.; Rheinwald, G.; Zsolnai, L.; Büchner, M.; Driess, A.; Huttner, G.; Strähle, J. Monomeric Alkyne-Stabilized Complexes of Organo−Copper(I) and −Silver(I). *Organometallics* **1999**, *18*, 598–605. [CrossRef]
51. Dias, H.V.; Flores, J.A.; Wu, J.; Kroll, P. Monomeric Copper(I), Silver(I), and Gold(I) Alkyne Complexes and the Coinage Metal Family Group Trends. *J. Am. Chem. Soc.* **2009**, *131*, 11249–11255. [CrossRef] [PubMed]
52. Chen, J.; London, H.C.; Pattadar, D.; Worster, C.; Salpage, S.R.; Jakubikova, E.; Saavedra, S.S.; Hanson, K. Increasing excited state lifetimes of Cu(I) coordination complexes *via* strategic surface binding. *Inorg. Chem. Front.* **2025**, *12*, 1295–1302. [CrossRef]
53. Englman, R.; Jortner, J. The Energy Gap Law for Non-Radiative Decay in Large Molecules. *J. Lumin.* **1970**, *1–2*, 134–142. [CrossRef]
54. Livshits, M.Y.; Turlington, M.D.; Trindle, C.O.; Wang, L.; Altun, Z.; Wagenknecht, P.S.; Rack, J.J. Picosecond to Nanosecond Manipulation of Excited State Lifetimes in Complexes with an Fe^{II} to Ti^{IV} Metal-to-Metal Charge-Transfer: The Role of Ferrocene-Centered Excited States. *Inorg. Chem.* **2019**, *58*, 15320–15329. [CrossRef]
55. Shields, G.C. Twenty years of exceptional success: The molecular education and research consortium in undergraduate computational chemistry (MERCURY). *Int. J. Quantum Chem.* **2020**, *120*, 26274. [CrossRef]